Evaluation of a tetramine-appended MOF for post combustion CO_2 capture from natural gas combined cycle flue gas by steam-assisted temperature swing adsorption

Yogashree Bharath, and Arvind Rajendran*

Department of Chemical and Materials Engineering, University of Alberta, Donadeo Innovation Centre of Engineering, 9211-116 Street NW Edmonton, Alberta, Canada T6G 1H9

July 7, 2023

*corresponding author: Arvind Rajendran, Phone: +1.780.492.3912, Email: arvind.rajendran@ualberta.ca

Abstract

A novel tetraamine-appended metal-organic framework (MOF), exhibiting double-stepped isotherm was explored in a 3-step steam-assisted temperature swing adsorption process (SA-TSA) for CO_2 removal from dry flue gas emitted from natural gas-fired power plants (NGCC). The reported material exhibited properties highly suited for CO_2 capture from dilute sources. Extensive numerical simulations were performed to comprehend the impact of isotherm shape, heat transfer coefficient, feed temperature and heat capacity of solid on adsorption and desorption dynamics in a fixed bed. A multi-objective optimization was performed to identify operating conditions that achieve low steam consumption and high productivity while maintaining high purity ($\geq 95\%$) and high recovery ($\geq 90\%$). It was found that high purity and high recovery are obtained only when the process is isothermal. Thermal fronts propagating through the column impact the process performance. We show that the process cannot achieve recovery targets, i.e., $\geq 90\%$, unless heat is removed from the system rapidly. The lowest achievable specific steam consumption is ≈ 45 $\mathrm{kg_{steam}\ kg_{CO_2}^{-1}}$ and highest achievable productivity is $\approx 0.1\ \mathrm{mol_{co_2}\ m_{adsorbent}^{-3}\ s^{-1}}$ in an isothermal scenario.

Keywords: CO_2 capture, tetramine-appended MOF, heat management, step-shaped isotherm.

1 Introduction

Anthropogenic greenhouse gases (GHGs), e.g. CO_2, result in climate change[1]. Multiple strategies are being pursued to mitigate GHG emissions[1]. These include replacing CO_2 intensive fuels, e.g., coal and oil, with less intensive ones, such as natural gas, in tandem with carbon capture and storage (CCS) solutions[2]. Natural gas combined cycle (NGCC) is a mature technology for power generation from natural gas. In this technology, natural gas is directly combusted in the presence of air to generate electricity. The flue gas from a typical NGCC plant is released at atmospheric pressure, at ≈60 - 110 °C and composed of ≈4-8 mol% CO_2, ≈8 mol% H_2O, ≈12 mol% O_2, traces of Ar with the balance being N_2[3]. Concentrating CO_2 from NGCC flue gas is challenging owing to the dilute amounts of CO_2 present in the gas. Absorption using liquid amines is energy-intensive[4]. Additionally, equipment corrosion and amine degradation int he presence of gases such as O_2 is a major concern[4]. Adsorption processes that employ solid sorbents for selective removal of CO_2 are a promising alternative[2]. Adsorption processes alternate between two key steps: the adsorption step, where the CO_2 is concentrated in the solid phase, and the regeneration step, where it is stripped off the solid. The regeneration is performed either by lowering the pressure, i.e., pressure swing adsorption (PSA) or increasing the temperature, i.e., temperature swing adsorption (TSA)[5,6]. Recent works have indicated that standalone- pressure/vacuum swing adsorption (PVSA) is unsuitable for dilute flue gas streams due to high energy consumption, high costs compared to liquid absorption technology and very low vacuum pressures[7,8]. For dilute CO_2 streams, to purify the heavy component, TSA processes seem favourable. A TSA process is operated as a fixed bed, moving bed or fluidized bed[9,10]. In the fixed bed mode, the sorbent remains stationary while the gas is routed through the bed to effect the separation. In moving bed mode, the adsorbent and gas stream is contacted in a continuous counter-current operation[11]. In a fluidized bed, the solid adsorbent is fluidized by the gas stream[11]. Fixed bed mode of operation results in low productivity owing to long cycle times resulting from the large thermal mass of the solid. Moving

and fluidized beds are promising alternatives as they cater to increased heat and mass transfer rates in a TSA system[9,10]. However, challenges related to the physical movement of solids, such as attrition and breakage, have posed challenges for scaling-up these processes. Recent results are showing promising advances towards commercialization[12].

Metal-organic frameworks (MOFs) are gaining popularity as potential CO_2 capture sorbents owing to their high surface area and adjustable pore chemistry[13,14]. Recently, Calgary framework-20 (CALF-20), a physisorbent MOF, has been manufactured at the tonne-scale and deployed for CO_2 capture from a cement plant using a fixed-bed process[15,16]. The impregnation of amine functional groups on MOFs has been explored in several studies to obtain high capacities at low partial pressures[13]. McDonald *et al.* reported diamine-appended MOFs that can behave as phase change materials with unusual single-step shaped isotherm[17]. The cooperative insertion mechanism of CO_2 into the MOF (with different metal centres like Mg, Mn, Fe etc.) resulted in high working capacities, and that too at low partial pressures of CO_2[13,17]. Recently, Kim *et al.* reported a novel tetramine appended MOF with an unusual double-step shaped isotherm[18]. The MOF exhibited multiple coordination of the metals and tetraamines, resulting in cyclic stability. These materials have high heat of adsorption ($\approx$99 kJ mol^{-1}) and high CO_2 capacity at low CO_2 partial pressures, high working capacity for a small swing in temperature, high thermal and oxidative stability, and high CO_2 selectivity over N_2. Kim *et al.* also reported that these materials show enhanced CO_2 capacity in the presence of water[18]. These materials demonstrated high oxygen, thermal, and amine stability due to the multiple metal coordination[18].

Amine-appended MOFs have been explored in the literature for process applications. Hefti *et al.* investigated the use of a diamine-appended MOF in a 4-step TSA cycle to separate CO_2 from a dry flue gas containing 12 mol% CO_2[19]. Detailed and shortcut models were used to simulate the TSA processes. It was shown that the diamine-appended MOFs in the 4-step TSA cycle required 22% less energy

and yielded 98% more productivity compared to the performance of a zeolite 13X employed in a 6-step TSA cycle[19]. The 4-step TSA cycle consisted of an external heating and cooling step. It was hypothesized that small temperature swings would suffice since the material showed a sharp change in the solid loading for a very small change in the temperature. However, it was also reported that temperature fronts in the column could reduce the solid phase CO_2 capacity, and operation near the inflection point should be avoided. Hence, the reduction in CO_2 capacity was avoided by selecting an appropriate range of temperature swings depending on the step's position and temperature. The effect of adsorption and regeneration temperatures on process performance was studied. It was found that the highest productivity was obtained for a significant difference between the two temperatures[19].

Pai *et al.* studied a 4-step vacuum swing adsorption (VSA) cycle for separation of CO_2 from a dry flue gas containing 15 mol% CO_2 using five different diamine-appended MOFs which differed in the metal center[20]. It was shown that the thermal fronts generated due to ad/desorption limit the accessible working capacity of the material. Although high CO_2 purities could be achieved, the ability to fully exploit the significant difference in the capacities for small changes in temperatures was not possible.

In another work by Fujiki *et al.*, equilibrium and kinetic parameters of a flexible MOF, ELM-11, that showed sigmoidal-shaped isotherms were studied[21]. The authors elucidated the relationship between the isotherm shape and the gate-opening property of the MOF. The breakthrough analysis was carried out experimentally and numerically modelled. It was found that the linear driving force model described the kinetics reasonably. Furthermore, it was found that the difference between the partial pressure of CO_2 and gate opening pressure affected mass transfer and slippage of CO_2. Very low mass transfer rates could significantly impact process designs[21]. In another work, the same authors explored the performance of ELM-11 in a 4-step VPSA process to separate CO2 from a 20% flue gas stream[22]. The work explores the effect of the sigmoidal isotherm and hysteresis on process performance. It was found

that process purity and productivity were higher than that of a zeolite 13X-based VPSA process. This was attributed to the high CO_2/N_2 selectivity of the MO. The study found that it was difficult to achieve high CO_2 recovery owing to CO_2 slippage when the CO_2 concentration is lower than the gate pressure.

Studies by Hughes *et al.* investigated the effect of temperature fronts in the column by simulating isothermal and adiabatic scenarios for CO_2 capture using a diamine-appended MOG[23]. It was found that a high spike in the temperature reduced the CO_2 loading. The work also indicated the need for heat removal associated with employing diamine-appended MOFs in a TSA process. The effect of bed temperatures, cooling times, and residence time of the flue gas in the column was investigated. It was found that cooling the bed helped improve bed utilization and CO_2 loading of the bed. Effective heat management reduced the cost of the TSA process.

TSA processes suffer from low productivity as there is a need to tackle the solid's thermal capacity. An effective regeneration mechanism capable of providing rapid heat exchange remains challenging. Various heating schemes have been explored in the literature. Clausse *et al.* explored the use of jacketed heating wire for regeneration[24]. Ntiamoah *et al.* reported TSA cycles employing indirect heating along with hot product gas purge for regeneration[25]. However, indirect heating techniques result in lower heat transfer rates and, hence, lower productivities than direct heating methods. Multiple studies have reported the benefits of a steam-assisted regeneration[10,18,26]. In this configuration, a condensable vapour, typically steam, is used as a stripping agent. The steam comes into direct contact with the sorbent and simultaneously increases the temperature and reduces the CO_2 partial pressure of CO_2.

The current work focuses on evaluating the performance of Mg_2(dobpdc)(tetramine) (abbreviated as Mg_2MOF) in a three-step steam assisted-TSA (SA-TSA) process. The adsorption equilibrium reported in the literature is described using an empirical function. Parametric studies that aim to understand the impact of the isotherm

shape on the process performance are reported. The SA-TSA cycle is optimized to maximize CO_2 purity and recovery. A rigorous optimization is then reported to maximize productivity and minimize the steam purge requirements. The ultimate goal of this work is to examine if the expected advantages of the isotherm shape translate into favourable process performance. We mainly explore an SA-TSA process as the MOF has been tested for steam stability, and commercial processes, e.g., from Svante Inc. that use steam regeneration, have already been scaled up for large-scale capture applications[16].

2 Modeling

2.1 Adsorption Equilibrium

Mg_2MOF, shows a unique double-stepped isotherm as seen in Fig. 1(a). The shape of the isotherm was attributed to the cooperative mechanism of CO_2 adsorption[18]. From the isotherm, the CO_2 capacity at a partial pressure of 0.04 bar is 1.3 mol kg^{-1} at 120 °C and as high as 3.4 mol kg^{-1} at 90 °C. A high working capacity of $>$ 1.2 mol kg^{-1} was also observed for a small swing in temperature from 100 to 120 °C. It can be seen that Mg_2MOF exhibited a high CO_2 heat of adsorption of 99 kJ mol^{-1} at low loadings. Figure 1(b) represents the variation of the heat of adsorption of CO_2 with solid loading. The presence of a step in Fig. 1(b) is reflective of the heat of adsorption corresponding to the two different steps of the isotherm, i.e., from 0 to $\approx$1.7 mol kg^{-1} and from $\approx$1.7 to $\approx$3.4 mol kg^{-1}. A type I isotherm model cannot be used to describe the unique isotherm shape. A weighted Langmuir isotherm model has been used in the literature to describe single-stepped isotherms[19,21]. In this work, we describe the CO_2 loading using an empirical model using a functional form that is similar to a recent work by Bingel and Walton[27].

$$q^*_{CO_2} = \arctan\frac{P}{b} + \frac{1.127}{1 + exp^{-s_1(P-m_1)}} + \frac{0.989}{1 + exp^{-1.283(P-m_2)}} \quad (1)$$

Here $q^*_{CO_2}$ is the equilibrium loading in mol kg^{-1}, P is the pressure of CO_2 in bar, b, s_1, m_1 and m_2 are fitting parameters that are described as a function of temperature T in K.

$$m_1 = 1.33 \times 10^{-13} \exp^{(0.0841T)} \tag{2}$$

$$m_2 = 1.24 \times 10^{-9} \exp^{(0.065T)} \tag{3}$$

$$s_1 = 1.74 \times 10^{11} \exp^{(-0.065T)} \tag{4}$$

$$b = 3.36 \times 10^{-10} \exp^{(0.0676T)} \tag{5}$$

Figure 1(a) shows the fitted isotherm model. It is worth emphasizing that while the isotherm model used here has no specific physical basis, it offers mathematical flexibility to capture the two steps in the isotherm and the temperature effect. We note that the experimental data is available between 90 - 120 ° C. However, flue gas temperatures are typically lower than these values, so extrapolation is required. Such an extrapolation at lower temperatures is shown in Fig. 1(a). The CO_2 heat of adsorption (ΔH), in kJ mol^{-1}) was fitted to the experimental equilibrium loading ($q^*_{CO_2}$) using the following equation:

$$\Delta H = 99 - \frac{24}{1 + \exp^{-50(q^*_{CO_2} - 1.6)}} \tag{6}$$

The comparison of the experimental ΔH data with the fitted model is shown in Fig. 1(b).

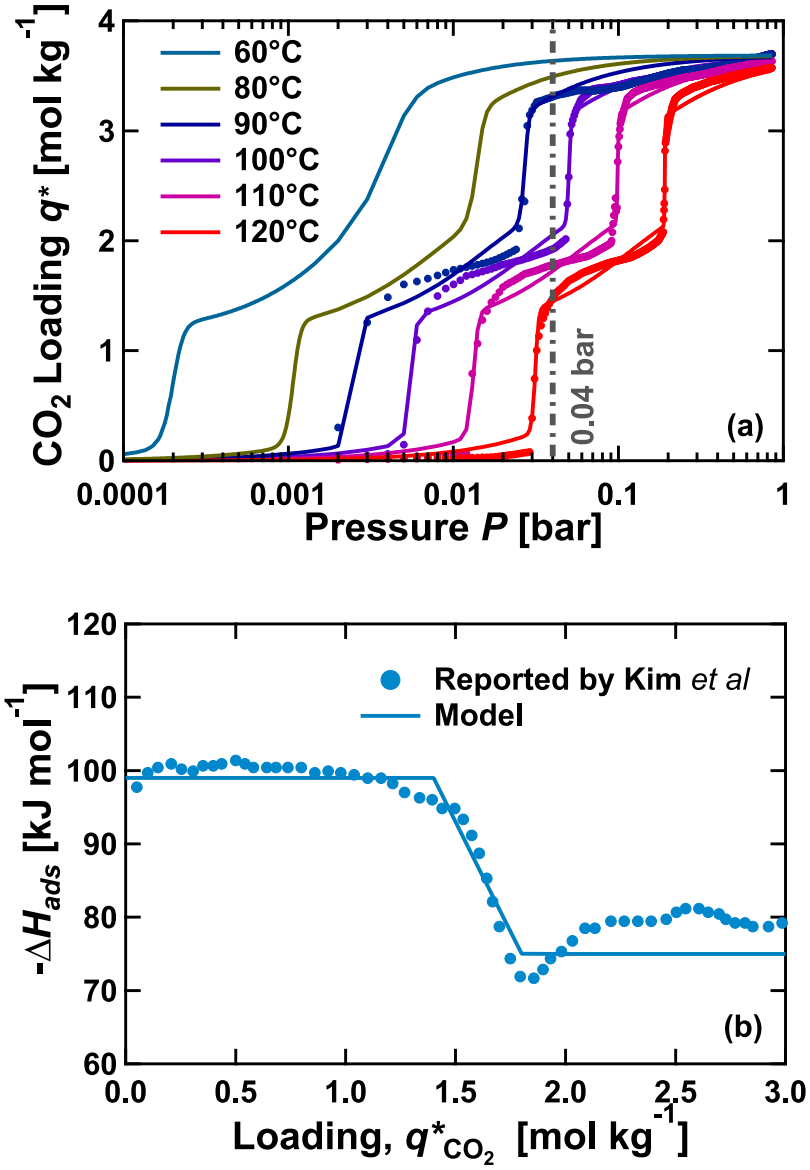

Figure 1: Adsorption equilibrium of CO_2 on Mg_2MOF. (a) CO_2 isotherms, (b) variation of the heat of adsorption of CO_2 with solid phase loading. Symbols represent experimental data reported by Kim *et al.*[18], and lines represent the fits.

The study by Kim *et al.* reported almost negligible N_2 adsorption on the MOF, and hence we assume N_2 adsorption is negligible[18]. Kim *et al.* also report the breakthrough curves and isobars of CO_2 adsorption on Mg_2MOF under humid conditions. The pure water isotherms on the MOF showed a single step. It was found that the CO_2 uptake remained stable in the presence of water. Although pure water adsorption isotherms are provided, sufficient information on competitive CO_2 isotherm data under humid conditions is unavailable. Hence this work assumes no adsorption of water or steam and treats them as inerts. The flue gas stream exiting the NGCC plant was also assumed to be free of SOx and NOx and O_2.

2.2 Modeling the TSA process

In this work, a non-isothermal and non-isobaric model was developed based on the following assumptions[28]:

- Gas phase can be described by the ideal gas law.
- No radial gradients exist and the column was considered one-dimensional.
- Uniform adsorbent properties across the bed
- Flow through column can be described by an axially dispersed plug flow model.
- Pressure drop was computed using Darcy's equation.
- Adsorption kinetics were defined by the linear driving force model (LDF).
- The solid and gas phases are in local thermal equilibrium.
- Heat transfer occurs across the column wall whose outer surface was maintained at a constant temperature.

Based on the above assumptions, the following transport equations can be written[5,28,29]. The component mass balance is given by:

$$\frac{\partial y_{\mathrm{i}}}{\partial t} = \frac{T}{P} D_{\mathrm{L}} \frac{\partial}{\partial z}\left(\frac{P}{T}\frac{\partial y_i}{\partial z}\right) - \frac{T}{P}\frac{\partial}{\partial z}\left(\frac{P y_{\mathrm{i}}}{T} v\right) - \frac{RT}{P}\frac{1-\epsilon}{\epsilon}\frac{\partial q_{\mathrm{i}}}{\partial t} - \frac{y_{\mathrm{i}}}{P}\frac{\partial P}{\partial t} + \frac{y_{\mathrm{i}}}{T}\frac{\partial T}{\partial t} \tag{7}$$

where y is the gas phase composition and, q is the solid loading of component i, v is the fluid phase interstitial velocity, ϵ is bed voidage, D_{L} is the axial dispersion, P is the pressure, T is the temperature and R is the universal gas constant. The total mass balance is given by:

$$\frac{1}{P}\frac{\partial P}{\partial t} = -\frac{T}{P}\frac{\partial}{\partial z}\left(\frac{P}{T} v\right) - \frac{RT}{P}\frac{1-\epsilon}{\epsilon}\frac{\partial q_{\mathrm{CO_2}}}{\partial t} + \frac{1}{T}\frac{\partial T}{\partial t} \tag{8}$$

It should be noted that the second term in the RHS of Eq. 8 contains only the contribution from CO_2 as other terms are considered to be inert.

The mass transfer between the solid and fluid phases was was described by the LDF model:

$$\frac{\partial q_{\mathrm{CO_2}}}{\partial t} = k(q^*_{\mathrm{CO_2}} - q_{\mathrm{CO_2}}) \tag{9}$$

where, k is the LDF coefficient.

The column energy balances is given by:

$$\begin{aligned}\left[\left(\frac{1-\epsilon}{\epsilon}\right)(\rho_{\mathrm{s}} C_{\mathrm{p,s}} + C_{\mathrm{p,a}} q_{\mathrm{CO_2}})\right]\frac{\partial T}{\partial t} &= \frac{K_{\mathrm{z}}}{\epsilon}\frac{\partial^2 T}{\partial z^2} - \frac{C_{\mathrm{p,g}}}{R}\frac{\partial}{\partial z}(vP) - \frac{C_{\mathrm{p,g}}}{R}\frac{\partial P}{\partial T} \\ &- \left(\frac{1-\epsilon}{\epsilon}\right) C_{\mathrm{p,a}} T \frac{\partial q_{\mathrm{CO_2}}}{\partial t} + \left(\frac{1-\epsilon}{\epsilon}\right)\left[(-\Delta H_{\mathrm{CO_2}})\frac{\partial q_{\mathrm{i}}}{\partial t}\right] - \frac{2h_{\mathrm{in}}}{\epsilon r_{\mathrm{in}}}(T - T_{\mathrm{w}})\end{aligned} \tag{10}$$

where ρ_{s}, and $C_{\mathrm{p,s}}$, are the density and heat capacity of the solid, respectively, $C_{\mathrm{p,a}}$ and $C_{\mathrm{p,g}}$ are the heat capacity of the adsorbed phase and fluid phase, respectively, K_{z} is the effective gas thermal conductivity, h_{in} is the inside heat transfer coefficient, r_{in} is the inner radius of the column, and T_{w} is the wall temperature. The wall energy balance is given by

$$\rho_{\mathrm{w}} C_{\mathrm{p,w}}\frac{\partial T_{\mathrm{w}}}{\partial t} = K_{\mathrm{w}}\frac{\partial^2 T_{\mathrm{w}}}{\partial z^2} + \frac{2 r_{\mathrm{in}} h_{\mathrm{in}}}{r^2_{\mathrm{out}} - r^2_{\mathrm{in}}}(T - T_{\mathrm{w}}) - \frac{2 r_{\mathrm{out}} h_{\mathrm{out}}}{r^2_{\mathrm{out}} - r^2_{\mathrm{in}}}(T_{\mathrm{w}} - T_{\mathrm{a}}) \tag{11}$$

where, ρ_{w}, and $C_{\mathrm{p,w}}$, are the density and heat capacity of the wall, respectively, K_{w} is the thermal conductivity of wall, h_{out} is the outside heat transfer coefficient, r_{out} is the outer radius of the column, and T_{a} is the ambient temperature.

Finally, the pressure drop in the system was given by Darcy's equation:

$$-\frac{\partial P}{\partial z} = \frac{150\mu(1-\epsilon)^2 v}{4\epsilon^2 r_{\mathrm{p}}^2} \tag{12}$$

where r_{p} is the radius of the solid particle and μ is the fluid viscosity. Darcy's law reasonably estimates the pressure drop for the column sizes considered in this work.

A finite volume (FV) technique, specifically, the van-Leer total variation diminishing (TVD) scheme. was used to reduce the partial differential equations (PDEs) to ordinary differential equations (ODEs). The resulting coupled ODEs were then solved using the *ode23s* solver in MATLAB until cyclic steady state was attained[28].

The MOF used in this work was assumed to be binderless, i.e., the equilibrium loading on the crystal is the same as that of the particle[20]. The specific heat capacity of the MOF was assumed to be in the range of the specific heat capacity of the diamine-appended MOFs reported by Hefti *et al.*[19] and Hughes *et al.*[23]. No kinetic information is available and hence, the LDF coefficient k used for the process simulations was a fixed numerical value. The particle voidage and bed voidage values were fitted by comparing the experimental breakthrough reported by Kim et al., with the curve obtained from the process simulation. Table 1 lists the parameters used in this work.

2.3 Process Configuration: Cycle Design

In this work, a 3-step SA-TSA process is considered. The process schematic is shown in Fig. 2.

The constituent steps of this cycle included an adsorption step, a counter-current

Table 1: Process simulation parameters

Parameter	Value	Source
Column Parameters		
Column length, L [m]	1	Standard value
Inner column radius, r_{in} [m]	0.14	Assumed
Outer column radius, r_{out} [m]	0.162	Assumed
Column void fraction, ϵ [-]	0.362	Fitted using bed density and particle voidage
Thermal conductivity of column wall, K_{w} [W m^{-1} K^{-1}]	16	Standard value for steel
Specific heat capacity of column wall, $C_{\text{p,w}}$ [J kg^{-1} K^{-1}]	502	Standard value for steel
Column wall density, ρ_{w} [kg m^{-3}]	7800	Standard value for steel
Particle Properties		
Particle voidage, ϵ_{p} [-]	0.58	Fitted to experimental breakthrough curve
Particle radius, r_{p} [m]	0.5×10^{-3}	Literature[18]
Tortuosity, τ [-]	3	Assumed
Crystal density, ρ_{c} [kg m^{-3}]	1000	Literature[18]
Particle density, ρ_{s} [kg m^{-3}]	420	Calculated from particle voidage and crystal density
Bulk density, ρ_{b} [kg m^{-3}]	267	Calculated from bed voidage and particle density
LDF coefficient for CO_2, k [s^{-1}]	0.005	Fitted to experimental breakthrough curve
Specific heat capacity of gas phase, $C_{\text{p,g}}$ [J kg^{-1} K^{-1}]	1010.6	Standard for CO_2
Specific heat capacity of adsorbed phase, $C_{\text{p,a}}$ [J kg^{-1} K^{-1}]	1010.6	Standard for CO_2
Specific heat capacity of adsorbent phase, $C_{\text{p,s}}$ [J kg^{-1} K^{-1}]	1400	Assumed
Fluid viscosity, μ [kg m^{-1} s^{-1}]	1.81×10^{-5}	Standard for CO_2
Molecular diffusivity, D_{m} [m^2 s^{-1}]	1.26×10^{-5}	Calculated from Chapman–Enskog
Effective gas thermal conductivity, K_{z} [W m^{-1} K^{-1}]	0.4	Assumed
Operational Parameters		
Inside heat transfer coefficient, h_{in} [W m^{-2} K^{-1}]	Variable	-
Outside heat transfer coefficient, h_{out} [W m^{-2} K^{-1}]	20000	Assumed
Universal gas constant, R [m^3 Pa mol^{-1} K^{-1}]	8.314	Standard value
Pressure, P_{H} [bar]	1	Assumed
Purge temperature, T_{pur} [°C]	120	Assumed
Specific heat of steam, $C_{\text{p,steam}}$ [kJ kg^{-1}]	2378	NIST Database

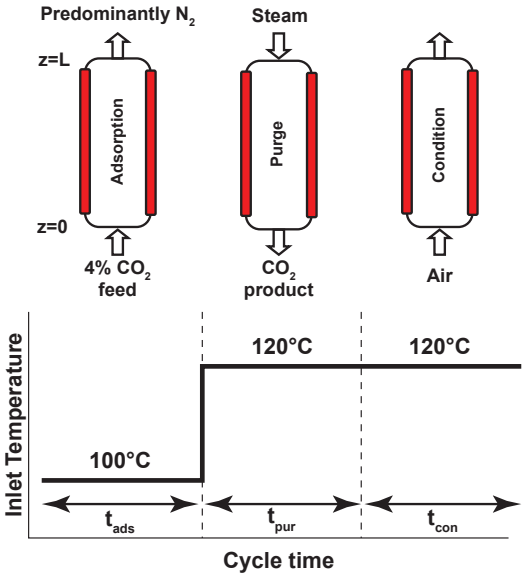

Figure 2: Process design configuration for 3-step SA-TSA.

steam purge and a conditioning step. These are described below.

- Adsorption: In this step, the dry flue gas containing 4 mol% CO_2 and 96 mol% N_2 is introduced at the inlet, i.e., $z = 0$, at 1 bar and 100 °C. The light product N_2 is removed at column exit, i.e., $z = L$.

- Purge: In this step, superheated steam is introduced at $z = L$, i.e., in a countercurrent direction, at 1 bar and at 120 °C. Product CO_2 is collected along with steam, at $z = 0$. We assume that steam does not condense within the column. The swing between feed temperature at 100 °C and purge temperature at 120 °C aids in desorbing the CO_2.

- Conditioning: In this step, hot air (modeled as N_2) is fed at $z = 0$, and at 1 bar and 120 °C. This step is used to remove any water that may potentially condense when coming into contact with the flue gas stream.

Note that the cycle chosen here is similar to the one employed for CO_2 capture from

cement flue gas[16]. The key performance indicators such as CO_2 purity (Pu), recovery (Re), steam ratio (SR) (a proxy for energy consumption) and productivity (Pr) are defined as follows:

$$\text{Purity, } Pu\,[\%] = \frac{\text{Total moles of } CO_2 \text{ in the product}}{\text{Total moles of } CO_2 \text{ and } N_2 \text{ in the product}} \times 100\% \tag{13}$$

$$\text{Recovery, } Re\,[\%] = \frac{\text{Total moles of } CO_2 \text{ in the product}}{\text{Total moles of } CO_2 \text{ fed}} \times 100\% \tag{14}$$

$$\text{Productivity, } Pr\,[\text{mol}_{CO_2}\ \text{m}^{-3}_{\text{adsorbent}}\ \text{s}^{-1}] = \frac{\text{Total moles of } CO_2 \text{ in the product}}{(\text{Total volume of adsorbent})(\text{Cycle time})} \tag{15}$$

$$\text{SteamRatio, } SR\,[\text{kg}_{\text{steam}}\ \text{kg}^{-1}_{CO_2}] = \frac{\text{Total mass of steam supplied to purge step}}{\text{Total mass of } CO_2 \text{ recovered}} \tag{16}$$

Purity in Eq. 13 is defined on a dry basis as water is assumed to be knocked out before product compression and cooling for transportation. The cycle time in the denominator of Eq. 15 represents the sum of the duration of the constituent steps. The mass of steam supplied to the purge step, as seen in Eq. 16, depends on the time of the purge step, the velocity of steam in the purge step, and the steam temperature. In this work, the steam temperature is kept at 120 °C to ensure no condensation within the column. The density of steam at 1 bar and 120 °C is used to compute the mass flowrate from the given volumetric flow rate.

2.4 Cycle Optimization

Cycle optimization was performed to identify operating conditions that result in the best possible process performance. The decision variables include adsorption time (t_{ads}), purge time (t_{pur}), conditioning time (t_{con}), and the feed velocity in each of the constituent steps, namely, (v_{ads}, v_{pur} and v_{con}). The ranges for the decision variables are provided in Table 2. The optimizations were carried out in two steps: The first involved an unconstrained optimization of maximizing purity and recovery. The

second step was constrained optimization to minimize the steam ratio and maximize productivity. A constraint of 95% purity and 90% recovery was imposed based on the U.S. Department of Energy (US-DOE) requirements. The optimization problems were solved using a non-dominated sorting algorithm (NSGA-II) technique[30]. The advantage of optimizing the cycle using NSGA-II was its ability to escape the local minima and ease of parallelization. The GA was run on MATLAB for 15 generations with a population size of 96. All computations reported were carried out on a desktop workstation with two 12-core Intel Xeon 2.5 GHz processors and 128 GB RAM and at Canada's Digital Research Alliance supercomputing facilities.

Table 2: Range of decision variables for process optimization studies

Decision Variable	**Range**
t_{ads} [s]	300 - 5000
t_{pur} [s]	300 - 8000
t_{con} [s]	300 - 2000
v_{ads} [m s^{-1}]	0.6 - 1
v_{pur} [m s^{-1}]	0.6 - 1
v_{con} [m s^{-1}]	0.6 - 1

3 Results and Discussion

3.1 Model Validation and Breakthrough Analysis

The experimental breakthrough data reported by Kim *et al.*[18] was used to validate the simulations of the fixed bed model. Figure 3 depicts breakthrough curves obtained from the experiments. The experimental conditions are provided in the caption. The model equations described in the previous section were solved under isothermal conditions. The isothermal conditions were reasonable, considering the

small size of the column. One can observe that the breakthrough curve consists of a shock wave-dispersed wave-shock wave transition. In other words, we observe a shock front at very low bed volumes, then a plateau followed by a second shock front. This differs from a simple shock wave transition of a type 1 isotherm (Langmuirian type)[31]. The unique breakthrough transition could be attributed to the isotherm shape. From Fig. 3, it can be seen that the breakthrough curve obtained by simulation captured the transitions reasonably well. However, a disparity between the experimental data and the simulated model is observed. The original paper did not provide any details about possible dead volumes in the system that can delay the experimental breakthrough curves. Nevertheless, the qualitative and near-quantitative match is considered a reasonable validation of the simulation model. The experimental breakthrough data were used to estimate the kinetic parameters for the adsorption of CO_2 on the Mg_2MOF. The LDF coefficient k_{CO_2} was varied within the simulation to match the shape of the breakthrough curve, leading to an estimate of $k_{CO_2} = 0.005 s^{-1}$.

The unique shape of the adsorption isotherm and the associated heat of adsorption is expected to generate strong thermal fronts that will travel across the column along with the mass fronts. To understand the interplay, we study the effect of the thermal nature of the column. We consider the inside heat transfer coefficient h_i to be a convenient parameter that can allow a variety of heat transfer scenarios. Three cases are considered: an isothermal condition represented by $h_i = 20000$ $W\,m^{-2}\,K^{-1}$; an adiabatic condition, using $h_i = 0$ $W\,m^{-2}\,K^{-1}$ and an intermediate case, called "non-isothermal" with $h_i = 10$ $W\,m^{-2}\,K^{-1}$. For the adsorption case study, the column is assumed to be filled with an inert gas at 1 bar pressure and 100°C. At the time $t = 0$, a feed gas consisting of 4 mol% CO_2 and the remaining inert gas is introduced at 100 °C. For desorption simulations, the column is assumed to be filled with 4 mol% CO_2 (and rest inert) at 100 °C, and at time $t = 0$, an inert at 100 °C is introduced to desorb the CO_2. The composition and temperature are calculated from the equations provided in the previous sections.

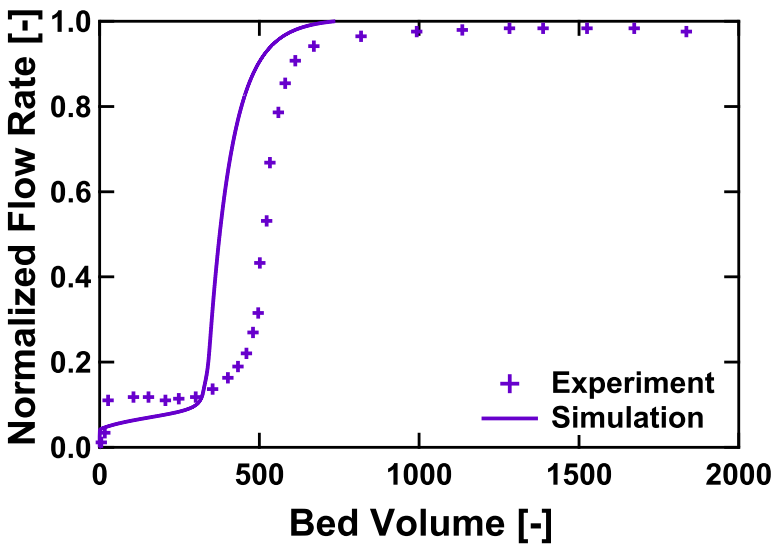

Figure 3: Pure component CO_2 breakthrough curves obtained from experiment (symbols) and simulation (line). The abscissa represents bed volume defined as $\frac{Qt}{V}$, where Q is the inlet volumetric flow rate, t is the time and V is the column volume. The ordinate represents normalized flow rate which is the ratio of flow rates of CO_2 at outlet to inlet of the column or $\frac{y_{CO_2,out}Q_{out}}{y_{CO_2,in}Q_{in}}$. The analysis was performed isothermally at a feed temperature of 100 °C, and flow rate of inlet gas, $Q_{in} = 30$ sccm as reported by Kim *et al.*[18]

Figure 4 shows the breakthrough curves for the three different thermal conditions. Figures 4(a) and 4(b) depict the composition and temperature breakthrough curves during adsorption, respectively. The transitions could be explained by the local equilibrium theory[31–33]. According to the theory, moving from the initial state (CO_2 partial pressure=0) to the feed state (CO_2 partial pressure=0.04 bar) results in three transitions. The adsorption starts with an anti-Langmuirian portion and progresses to an inflection point, after which it displays Langmuirian-type behaviour. The wave propagation between these three regions gives rise to the corresponding, complex shock-wave-shock transition. The desorption breakthrough under isothermal conditions (Fig. 4(c)), can also be similarly explained[33].

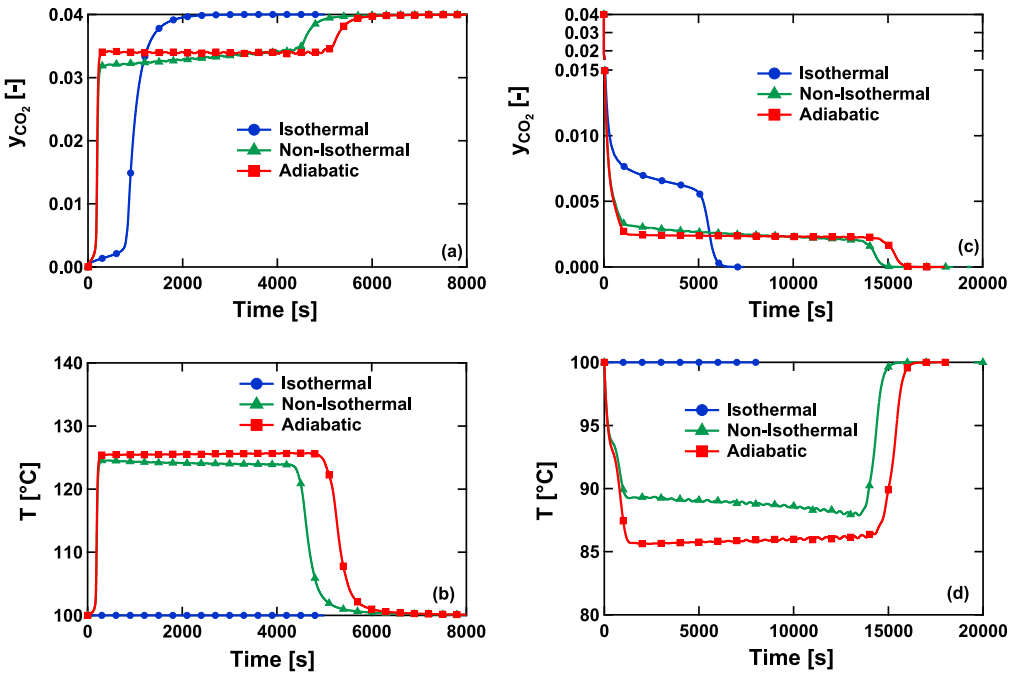

Figure 4: Effect of heat transfer rates on CO_2 breakthrough. (a) CO_2 breakthrough during adsorption, (b) Temperature breakthrough during adsorption, (c) CO_2 breakthrough during desorption, (d) Temperature breakthrough during desorption. Operating conditions: feed temperature = 100 °C, Total pressure = 1 bar, Inlet gas velocity = 1 m s^{-1}. Other column characteristics are given in Table 1.

Under adiabatic and non-isothermal modes, the adsorption and desorption breakthrough curves are markedly different from the isothermal case. From Fig. 4(a) it can be seen that CO_2 breaks through much earlier than the isothermal case. The second discontinuity under the isothermal case occurs at 1000 s compared to the non-isothermal case, where it happens at 4500 s, while for the adiabatic case, it is at 5500 s. The difference between the breakthrough curves can be rationalized by observing the thermal fronts that are generated (c.f. Fig. 4(b)). Under isothermal conditions, the temperature in the column remains constant, i.e., the heat transfer rate is instantaneous. However, in the adiabatic case, the heat is not dissipated to the surroundings. The heat released due to adsorption, thus gets trapped within the

column until the temperature front exits the column. This can be seen in Fig. 4(b) as a sharp surge in the temperature from 100 °C to 125 °C. The surge in temperature results in a sharp reduction in CO_2 loading as seen from Fig. 1(a). Due to a reduction in the bed's capacity, the velocity of the concentration wave fronts increases, thereby resulting in an early breakthrough of CO_2 at 3.5 mol% CO_2. The capacity is restored as the thermal wave passes through the column, and the final breakthrough occurs.

From Fig. 4(c), it can be observed that it takes the shortest time to completely regenerate the bed in an isothermal case compared to the adiabatic and non-isothermal modes of operation. It takes approximately 5000 s and 20000 s to completely clean the bed in isothermal and adiabatic modes of operation, respectively. During desorption, as seen in Fig. 4(d), there is a drop in temperature to 85 °C. This is attributed to the high heat of adsorption that cools the bed. This drop in temperature results in an increase in CO_2 loading from the isotherm as in Fig. 1(a). The concentration wave moves slower, thus resulting in a long time to clean the bed. Under the non-isothermal scenario, the heat transfer rate is higher than that of the adiabatic scenario but lower than the isothermal case; thus, the discontinuity is observed at a time in between the two other cases. Since flue gas from NGCC plants consists of 4 - 8 mol% of CO_2 [3], breakthrough curves were analyzed for feed conditions consisting of 5 mol% and 8 mol% CO_2 under isothermal, non-isothermal and adiabatic modes of operation. It is worth noting that the feed conditions at 5 mol% rest on the second inflection point of the isotherm, and the 8 mol% rests on the second step. The results of these studies are provided in the supplementary information. Figures S1(a) and S1(b) indicate the adsorption and desorption breakthrough curves for 5 mol% CO_2 and Fig. S1(c) and S1(d) indicate the adsorption and desorption breakthrough curve for 8 mol% CO_2. Although the change in feed composition is small from 4 mol% to 5 mol%, the breakthrough transitions in the adiabatic and non-isothermal modes of operation (as seen in Fig. S1(b)) during desorption is different for 5 mol% as compared to that of 4 mol%. This is because the 5 mol% feed lies on the second inflection region of the isotherm. However, the desorption times for the adiabatic modes (and non-isothermal) of operation in Fig. 4(c) and Fig. S1(b) are similar. From Figs. S1(c)

and (d), it can be observed that the breakthrough transitions change according to the location of the feed step, in this case, the second step of the isotherm. Thus, it can be concluded that the position of the feed composition on the isotherm and heat transfer coefficients impact the breakthrough transitions.

3.2 Effect of feed temperature on breakthrough

From the previous section, it is clear that temperature fronts play an important role in the adsorption and desorption dynamics in the column. The flue gas temperatures from NGCC plants are typically in the range of 60 - 110 °C[3]. Hence, exploring the effect of the feed temperature on the column dynamics is pertinent. The impact of feed temperature on the CO_2 adsorption breakthrough and CO_2 regeneration is described in Fig. 5. This study was conducted for isothermal and adiabatic modes of operation. In each of these cases, the column is assumed to be filled with an inert at the temperature of interest, and 4 mol% of CO_2 enters at the same temperature for the adsorption study. For desorption runs, the column is originally saturated with 4 mol% CO_2 at the temperature of interest and purged with an inert at the same temperature.

From Fig. 5, it is evident that the change in feed temperature influences the shape and elution time of the breakthrough curve. As feed temperature increases, one would expect the CO_2 capacity to decrease, decreasing adsorptive breakthrough time. In the isothermal mode of operation, as seen in Fig. 5(a), it can be observed that the breakthrough time is the lowest for a feed temperature of 100 °C. The breakthrough time for a feed temperature of 60 °C and 80 °C is comparable. For a feed temperature of 60 °C and 80 °C, the position of the feed rests on the second step of the isotherm, as seen in Fig. 1(a). At this point, the CO_2 capacities are similar. This implies that the concentration fronts move with approximately the same velocity. For a feed temperature of 100 °C, the feed is located on the first step of the isotherm, as seen in Fig. 1(a), indicating lower capacity than that at 60

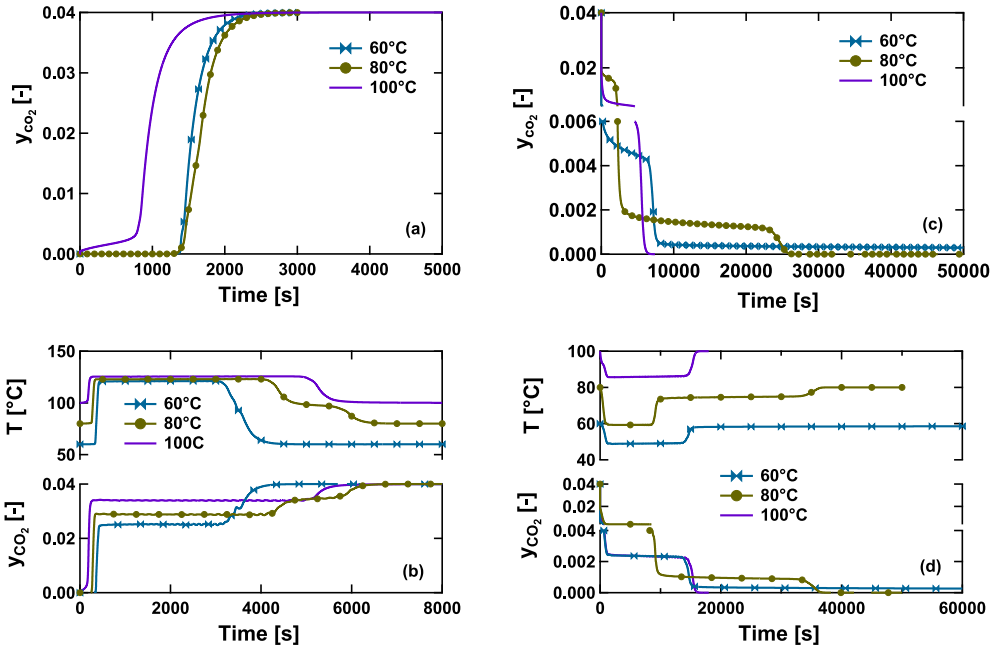

Figure 5: Adsorption and desorption breakthrough curves at different feed temperatures and different modes of operation. Sub-figures (a) and (b) show the adsorption breakthrough curve with varying feed temperatures under an isothermal and adiabatic mode of operation, respectively. Sub-figures (c) and (d) show the corresponding results during desorption. Sub-figures (b) and (d) consist of two panels each, the bottom indicating composition curves at the exit of the column and the top indicating corresponding temperature history. These studies were performed at a CO_2 feed composition of 4 mol%, 1 bar pressure, velocity of inlet gas = 1 m s^{-1}, and rest of the column characteristics are given in Table 1.

°C and 80 °C. This results in faster-moving concentration fronts and, thus, shorter breakthrough time. During desorption, as shown Fig. 5(c), it can be seen that the time required to completely regenerate the bed decreases with an increase in feed temperature. It takes the longest time to purge the column with a feed temperature of 60 °C, followed by 80 °C and 100 °C, respectively. Although the feed rests on the second step for a feed temperature of 60 °C and 80 °C, the wave velocities of the

concentration fronts during desorption are different. At a feed temperature of 60 °C, the concentration wavefront moves the slowest resulting in longer times to purge the bed than at 80 °C. For a feed temperature of 100 °C, the concentration wavefronts move faster, resulting in reduced time to regenerate the bed.

In the adiabatic scenario, as shown in Fig. 5(b), it can be seen that the adsorption breakthrough time reduces with an increase in feed temperature. This is because the thermal fronts break through fastest at a feed temperature of 60 °C, followed by 80 °C and 100 °C, respectively. This implies that the CO_2 capacity is highest for a feed temperature of 60 °C and lowest for that at 100 °C. Thus, the amount of CO_2 that escapes the column due to the propagation of thermal wavefronts is the lowest for 60 °C and highest for that at 100 °C. This implies that the time required to completely clean the bed is the longest at 60 °C. This effect can be seen in Fig. 5(d). It can also be seen that the low capacity for a feed temperature of 100 °C results in the least time to regenerate the bed.

From the above plots and analysis, it can be summarized that feed temperature significantly impacts column dynamics. Adjusting the feed temperature could help alter the bed's capacity and thus inherently alter the time required to regenerate the bed. By altering the time required to clean the bed completely, one can select appropriate purge times in a process cycle that may help maximize the process performance.

3.3 Effect of adsorbent heat capacity ($C_{p,s}$) on breakthrough

The original paper from Kim *et al.* does not provide any information about the heat capacity of the MOF. Hence, in this work, the heat capacity is assumed to be around 1400 $J\,kg^{-1}\,K^{-1}$ similar to that of a diamine appended MOF as reported by Hefti *et al.*[19]. Since the previous simulations demonstrate the impact of thermal fronts, it is necessary to understand the impact of the solid heat capacity, $C_{p,s}$ on

the wave propagation. The wave velocity of the temperature front is a function of heat capacity of the solid[5,6,31,32]. Recently Moosavi *et al.* used atomistic simulations to estimate the range of heat capacities that MOFs exhibit[34]. It was shown that MOFs indicate a wide range of specific heat capacities from 400 - 1300 $\mathrm{J\,kg^{-1}\,K^{-1}}$ for different crystal densities[34]. Since the assumed value of $C_{\mathrm{p,s}}$ of 1400 $\mathrm{J\,kg^{-1}\,K^{-1}}$ is close to the upper band of the values reported by Moosavi *et al.*, the adsorption breakthrough curves and desorption profiles are investigated for lower heat capacity values.

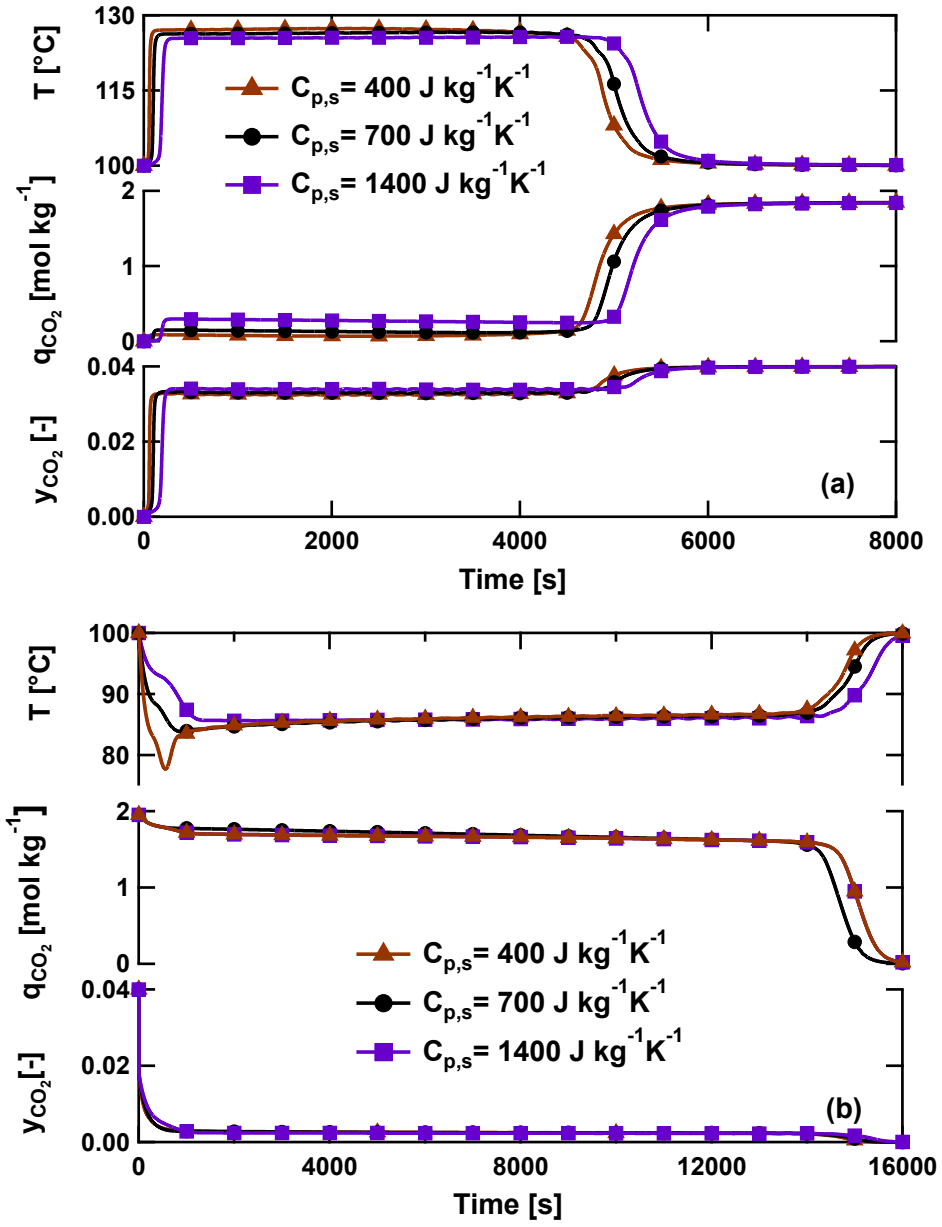

Figure 6: Effect of varying heat capacity of adsorbent on column dynamics. (a) adsorption breakthrough curves, (b) desorption curves. These studies were performed at a CO_2 composition of 4 mol%, velocity of inlet gas = 1 m s^{-1}, 1 bar pressure, feed temperature of 100 °C and other column properties are given in Table 1.

A case study was performed by using $C_{p,s}$ values of 400 and 700 J kg^{-1} K^{-1} and the results are shown inFig. 6. Two important observations can be made from Fig. 6(a) and Fig. 6(b). Firstly, $C_{p,s}$ affects the velocity of the thermal fronts. From the figures, it is clear that the thermal front associated with a lower $C_{p,s}$ value travels faster than that with a higher $C_{p,s}$ value. Secondly, there is almost no change in the adsorption and desorption dynamics for a large change in $C_{p,s}$ value. Let us consider the effect of $C_{p,s}$ on the adsorption dynamics as seen in Fig. 6(a). For a change in $C_{p,s}$ from 1400 to 400 J kg^{-1} K^{-1}, i.e., a 3.5× reduction,one would approximately expect a ΔT ratio of 3.5. However, from Fig. 6(a), it can be seen that for a change in $C_{p,s}$ from 1400 to 400 J kg^{-1} K^{-1}, a ΔT of 5.5 °C and 7 °C is observed respectively, i.e, a ΔT ratio of 1.27 is observed. This ratio is lower than the expected value. Such an observation can be understood by realizing that the change is temperature is also related to the change in solid phase loading. In typical Langmuirian systems, depending on the heat of adsorption of CO_2, there is a moderate change in loading q, with temperature T. In the current case, a small variation in temperature, especially around inflection points, has a substantial effect on the loading, as seen in the middle panel of Fig. 6(a). This reduces the effective heat that is released. Thus, varying the $C_{p,s}$ by a factor of 10 does not impact the performance. Similarly, the effect of $C_{p,s}$ and temperature on loading can be explained during desorption as seen in Fig. 6(b). From this study, it can be summarized that while altering $C_{p,s}$ impacts the movement of temperature fronts, the impact on the breakthrough dynamics seems minimal, at least in the region we have studied. Since changes in $C_{p,s}$ values do not alter the adsorption/desorption dynamics significantly, variation of $C_{p,s}$ will not be investigated further in this work.

Other material properties, such as the density of the adsorbent, are expected to alter adsorption and desorption dynamics in the column. The effect of solid density, ρ_s on the column dynamics, under isothermal and adiabatic modes of operation, is presented in Fig. S2. The ρ_s of Mg_2MOF is reported as 420 kg m^{-3} [18]. Additionally, density values of ρ_s = 210 and 840 kg m^{-3} are considered for this study. During adsorption under both modes of operation, as shown in Fig. S2(a) and Fig. S2(c),

it can be seen that a higher ρ_s, results in delayed CO_2 breakthroughs. This is because, at higher ρ_s values, more amount of adsorbent can be packed into the column, thereby increasing the CO_2 capacity and hence delayed breakthrough times. Similarly, during desorption, as shown in Fig. S2(b) and Fig. S2(d), higher ρ_s values results in longer times to completely clean the bed. This is also attributed to the increased CO_2 capacity, affecting the time required to regenerate the bed. These studies indicate that material properties of the Mg_2MOF are pivotal to evaluate the material's breakthrough dynamics and its process performance.

3.4 Process Simulation: Parametric studies

In the previous section, we have seen the impact of key operating conditions and material properties on breakthrough transitions. We now turn our attention toward understanding process dynamics. The goal here is to study the impact of the operating conditions on the performance indicators, namely purity and recovery. The process simulation was carried out for 4 mol% CO_2 feed composition and restricted to isothermal and adiabatic modes of operation, as these are more illustrative. The operating conditions are shown in the caption of Fig. 7. Fixed adsorption and desorption times were used to simplify the comparison. The cycle shown in Fig. 2 was simulated until the system reached a cyclic steady state. The isothermal mode of operation results in a $Re = 83\%$, and $Pu = 97\%$, while the corresponding values for the adiabatic mode of operation are $Re = 21\%$ and $Pu = 90\%$, respectively. Although there is only a small difference in the purity values, there is a notable difference in the recovery. This difference can be explained using the profiles shown Figs. 7(a) and 7(b). While interpreting the profiles, it is important to note that the gas inlet for the adsorption and conditioning steps is at $z/L = 0$, while for the purge step, it is at $z/L = 1$. Under the isothermal case, no active temperature front propagates through the column. Hence, more than 80% of the bed is loaded with CO_2 as seen in the adsorption loading profile of Fig. 7(a). The corresponding gas phase profile also indicates that most of the column was saturated with CO_2. From the loading

profiles at the end of the purge step, as shown in Fig. 7(a), it is clear that more than 80% of the bed is regenerated. This can also be visualized in the gas phase profiles, which indicate the low composition of CO_2 in the column. Also, there is less significant adsorption/desorption in the conditioning step. Since the bed's capacity is preserved with most of the CO_2 being recovered, a high recovery is obtained from the isothermal mode of operation.

Under the adiabatic mode of operation, as illustrated in Fig. 7(b), the retention of heat within the column and the high heat of adsorption establishes a thermal front across the column. The rise in temperature from 100 °C to 130 °C reduces the CO_2 capacity. The bed's capacity drops as soon as the temperature surge is encountered, thus resulting in a small portion of the bed being utilized in the adsorption step. Since the bed capacity is lowered, much of the CO_2 fed exits the column along with the N_2. The gas phase profiles of the adsorption step in Fig. 7(b) indicate that CO_2 is lost from the column outlet during the adsorption step. The driving force for desorption in the adiabatic case is a combination of concentration and temperature swings. From the loading profiles of the purge step of Fig. 7(b), the lower recovery of CO_2 is attributed to the loss of CO_2 in the adsorption step (due to the reduced capacity of the bed). It must be noted high purities are achievable for the conditions studied, irrespective of the mode of operation. Due to the high selectivity of CO_2 over N_2, less amount of N_2 is collected in the product, and hence the product purity is high. From the sample cycle simulation, it is worth mentioning that the active heat fronts reduce CO_2 capacity, decreasing the bed utilized, thus resulting in reduced recovery.

The same sample cycle simulation was repeated for three different feed temperatures to understand the effect of changing feed temperature on process dynamics. Table 3 summarises the key performance indicators achieved with different feed temperatures. It shows that high purities are achievable for a specific process condition irrespective of feed temperature. However, the impact of feed temperature on recovery is different for the isothermal case compared to the adiabatic case. In the

isothermal operation, the recovery increases with feed temperature and then drops. On the contrary, the recovery consistently drops with increasing temperature for the adiabatic case.

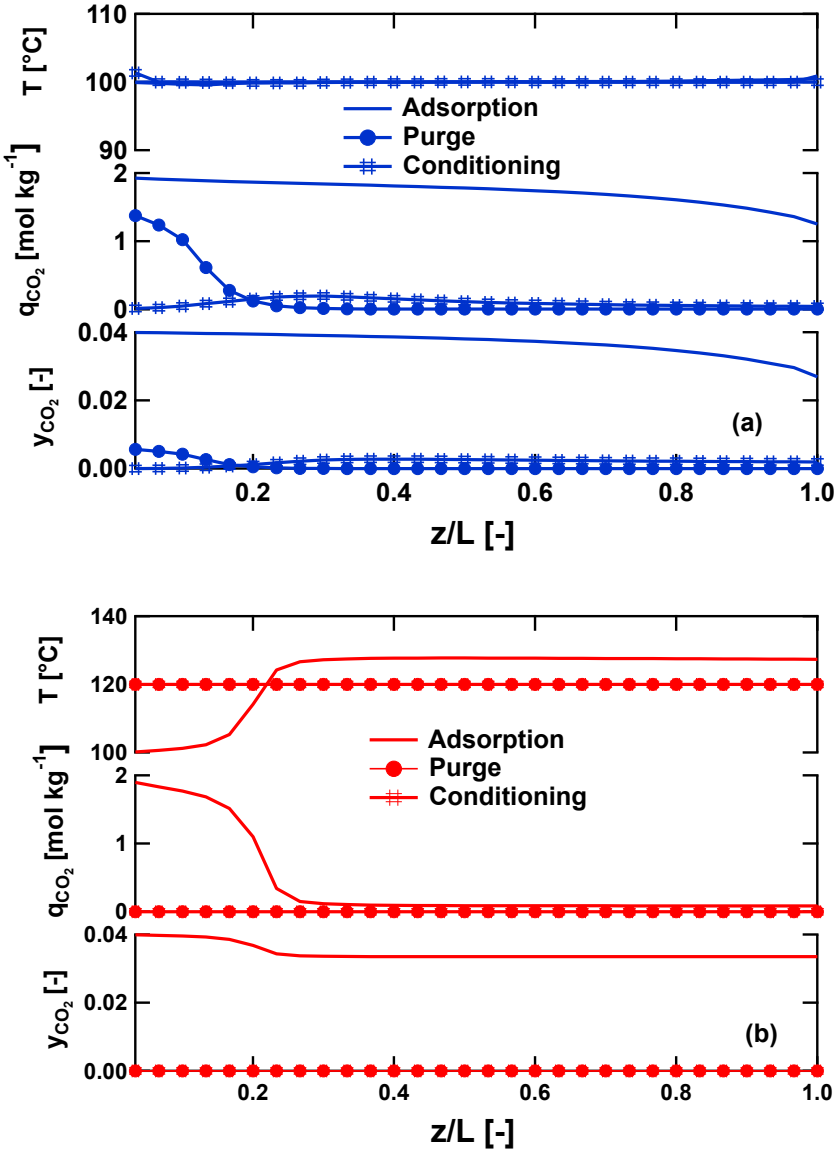

Figure 7: Results of three-step s-TSA process. Gas phase composition, solid phase loading and temperature profiles for (a) isothermal mode of operation, and (b) adiabatic mode of operation. The profiles are shown at the end of each step after the process has reached CSS. The simulation was performed for $t_{\mathrm{ads}} = 1000$ s, $t_{\mathrm{pur}} = 5000$ s, $t_{\mathrm{con}} = 1000$ s, $v_{\mathrm{ads}} = 1\ \mathrm{m\,s^{-1}}$, $v_{\mathrm{pur}} = 1\ \mathrm{m\,s^{-1}}$, $v_{\mathrm{con}} = 1\ \mathrm{m\,s^{-1}}$ with adsorption proceeding at 100 °C and steam purge and conditioning 100 °C for isothermal mode and 120 °C for adiabatic mode.

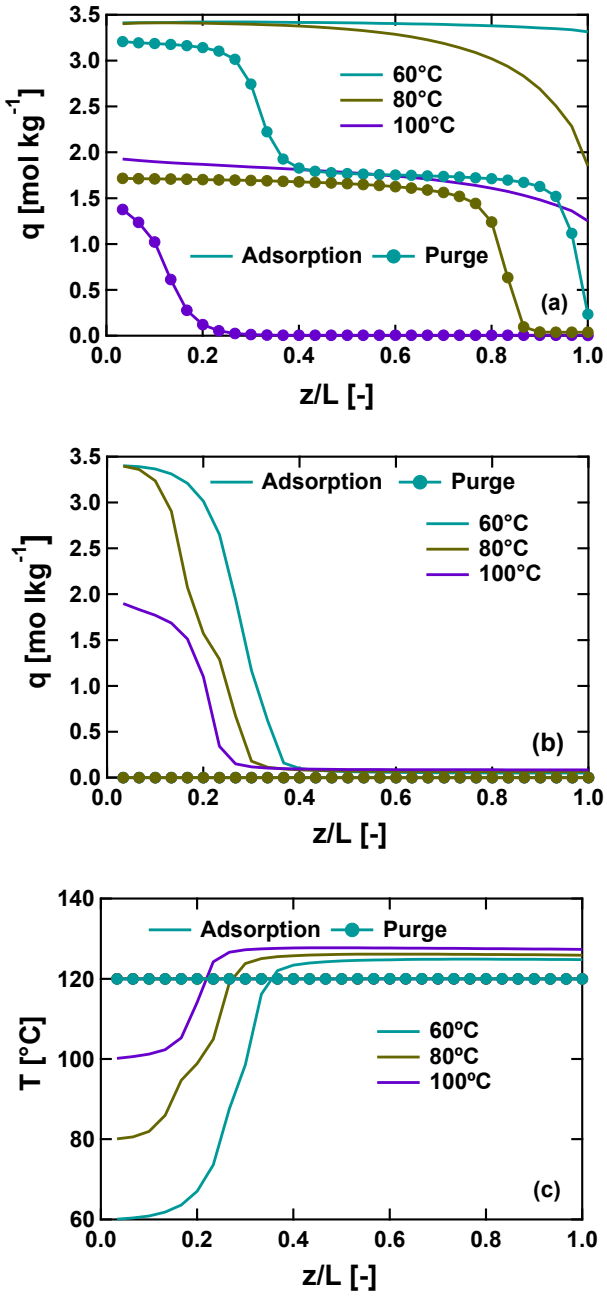

Figure 8: Solid phase loading and temperature profiles for isothermal and adiabatic modes of operation with varying feed temperature. (a) CO_2 loading profile under the isothermal scenario, (b) and (c) CO_2 loading and temperature profiles under the adiabatic scenario. The profiles are shown at the end of each step after the process has reached CSS. In all figures, solid lines represent profiles in the adsorption step, and circular markers indicate the profiles in the purge step. These profiles correspond to $t_{\text{ads}} = 1000$ s, $t_{\text{pur}} = 5000$ s, $t_{\text{con}} = 1000$ s, $v_{\text{ads}} = 1\ \text{m s}^{-1}$, $v_{\text{pur}} = 1\ \text{m s}^{-1}$, $v_{\text{con}} = 1\ \text{m s}^{-1}$. Performance indicators for these conditions are provided in Table 3.

Table 3: Process performance indicators for varying feed temperature (T_{feed}) and modes of operation. The process conditions are $t_{\text{ads}} = 1000$ s, $t_{\text{pur}} = 5000$ s, $t_{\text{con}} = 1000$ s, $v_{\text{ads}} = 1\ \text{m s}^{-1}$, $v_{\text{pur}} = 1\ \text{m s}^{-1}$, $v_{\text{con}} = 1\ \text{m s}^{-1}$.

Mode	T_{feed} [°C]	Pu [%]	Re [%]	SR [$\text{kg}_{\text{steam}}\ \text{kg}_{\text{CO}_2}^{-1}$]	Pr [$\text{mol}_{\text{CO}_2}\ \text{m}_{\text{adsorbent}}^{-3}\ \text{s}^{-1}$]
Isothermal	60	99	62	83	0.078
	80	99	91	56	0.1
	100	97	83	58	0.094
Adiabatic	60	95	42	100	0.055
	80	94	33	136	0.04
	100	90	22	224	0.024

In the isothermal mode of operation, as in Fig. 8(a), the front nearly breaks through the column in the adsorption step for all feed temperatures. It must be noted that the CO_2 loading corresponds to the second step in the isotherm in the case of 60 °C and 80 °C, while it corresponds to the first step in the case of 100 °C as explained previously. In the purge step, the bed is not fully regenerated for the duration chosen. Considering the progression of the front in the adsorption step, it can be seen that the front has broken through in the case of 60 °C leading to recovery loss. This effect is mitigated in the case of 80 °C; hence, the recovery is improved. For the case of 100 °C, the feed is located on the first step of the isotherm, and this causes a loss of CO_2 in the adsorption step and recovery decreases. From this study, it can be seen that altering feed temperature impacts process dynamics and performance indicators.

In the adiabatic scenario, an increasing feed temperature results in a lower recovery. These trends can be understood by considering the loading, and the corresponding temperature profiles shown in Fig. 8(b) and Fig. 8(c), respectively. From Fig. 8(b), it is clear that most amount of CO_2 is trapped at a feed temperature of 60

°C followed by 80 °C and 100 °C. The purge step ensures that all the trapped CO_2 is removed from the column. The corresponding temperature profiles are shown in Fig. 8c). The surge in temperature due to high heat of adsorption of CO_2 and the movement of these heat fronts influence the CO_2 capacity of the bed. Therefore, it can be inferred that higher CO_2 capacity results in higher bed utilization, and thus, more CO_2 is extracted at the end of regeneration. Hence the CO_2 recovery decreases as temperature increases.

Thus, from these parametric studies, it can be concluded that heat fronts hamper the bed's capacity, thus reducing CO_2 recovery. High purities can be accomplished in all cases owing to the practically infinite CO_2/N_2 selectivity, but achieving high recovery seems challenging, particularly under the adiabatic mode of operations. To explore if the process performance can be improved, we proceed to thorough process optimization.

3.5 Process Optimization

A process optimization strategy was employed to explore a wider set of conditions. As mentioned earlier, the optimization was carried out in two steps. In the first study, purity and recovery were maximized simultaneously, i.e., the objective functions were:

$$\min J_1 = \frac{1}{Pu_{CO_2}} \tag{17}$$

$$\min J_2 = \frac{1}{Re_{CO_2}} \tag{18}$$

In the second study, the minimization of the steam ratio and the maximization of productivity, subject to purity and recovery constraints, was considered. The objective functions here were formulated as follows:

$$\min J_3 = SR + \lambda_1 max[0, Pu_{\text{target}} - Pu_{\text{CO}_2}]^2 + \lambda_2 max[0, Re_{\text{target}} - Re_{\text{CO}_2}]^2 \quad (19)$$

$$\max J_4 = \frac{1}{Pr} + \lambda_1 max[0, Pu_{\text{target}} - Pu_{\text{CO}_2}]^2 + \lambda_2 max[0, Re_{\text{target}} - Re_{\text{CO}_2}]^2 \quad (20)$$

where λ_1 and λ_2 are penalty factors, Pu_{target} and Re_{target} are the targets specified that need to be achieved. In our case $Pu_{\text{target}} \geq 95$ and $Re_{\text{target}} \geq 90$.

For the optimization problem, six operating parameters t_{ads}, t_{pur}, t_{ads}, v_{ads}, v_{pur} and v_{con} were considered as decision variables. The range of the decision variables is provided in Table 2 and the results are shown in Fig. 9. The Pareto curves represent the best possible trade-off of purity-recovery in Fig. 9(a) and steam ratio-productivity in Fig. 9(b). It must be noted that each point on the Pareto curve is a unique combination of decision variables that yield the best possible trade-off between the opposing objectives.

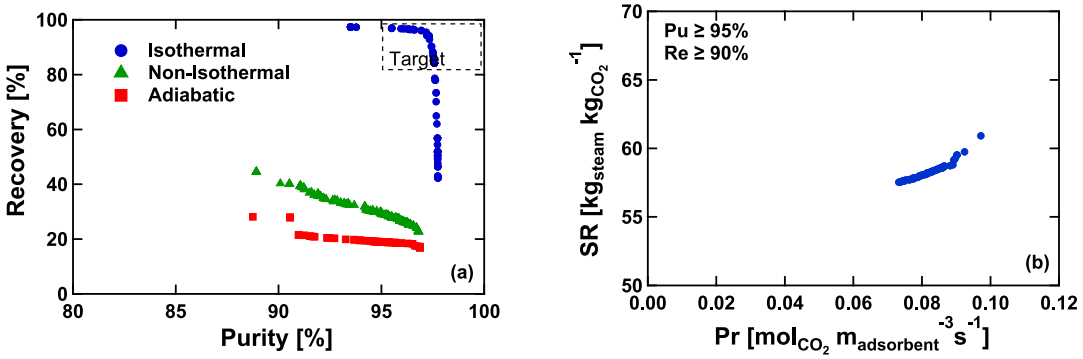

Figure 9: Pareto curves from process optimization for a feed temperature of 100 °C. (a) Pareto curve obtained from multi-objective optimization to simultaneously maximize CO_2 purity and recovery for the three modes of operation and (b) Pareto curve obtained from the minimization of steam ratio and maximization of productivity for isothermal mode of operation under the constraints Pu $\geq$ 95% and Re $\geq$ 90%.

From Fig. 9(a), it can be seen that running the cycles isothermally yields a high

CO_2 purity ($\geq 95\%$) and high recovery ($\geq 90\%$). Although a high CO_2 purity of $\geq 95\%$ was obtained under non-isothermal and adiabatic modes of operation, the recovery values were very low. A maximum recovery of 40% and 25% was obtained in non-isothermal and adiabatic modes of operation, respectively, with high purity $\geq 95\%$. Higher recoveries may be achieved for a different decision variable space. The low recoveries in non-isothermal and adiabatic cases were related to active temperature fronts and heat propagation in the system. High recoveries in the isothermal case were due to the absence of thermal effects.

The steam consumption - productivity optimization results are shown in Fig. 9(b). Since the non-isothermal and adiabatic cases did not meet the purity-recovery constraints, their steam ratio-productivity Pareto curves were not computed. Under the isothermal mode of operation, it can be seen that maximum productivity of 0.1 $\mathrm{mol_{CO_2}\ m^{-3}_{adsorbent}\ s^{-1}}$ and lowest possible steam ratio of $\approx$ 56 $\mathrm{kg_{steam}\ kg^{-1}_{CO_2}}$ is obtained. In this work, a high steam ratio and low productivity are attributed to the long purge times required by the system. High steam ratios are also attributed to the cycle design. Although the isothermal mode of operation is the most beneficial method to run the 3-step SA-TSA process cycle with a Mg_2MOF, it appears it might still be a disadvantage owing to the long purge times, high steam ratios and low productivities. It is to be noted that the steam consumption, in this case, should be read while noting that the product CO_2 is obtained as a mixture of CO_2 and superheated steam. Potentially this steam can be condensed, its heat recovered, and the CO_2 concentrated. Hence a direct comparison with other capture techniques should be made with caution.

The decision variables are mapped to the corresponding performance indices at optimum conditions in Fig. S3 of the supporting information. From Fig. S3(a), it can be inferred that long adsorption times are needed for high purities for all modes of operation. Long adsorption time ensures eluting most of the CO_2 that may be present in the void spaces, thereby improving purity (as seen from the recovery plots). However, long adsorption times reduce CO_2 recovery as there is increased

loss of CO_2 in the adsorption step due to increased operating time. Hence, it can be seen that lower adsorption times aid in achieving higher recoveries. It must be noted that the optimizer moves towards larger purge times and shorter adsorption times in order to maximize purity and recovery for all scenarios. From Fig. S3(b), higher productivities are obtained for shorter adsorption times. Shorter adsorption times result in shorter cycle times and, thereby, higher productivities. Figure S3(c) indicates that longer purge times result in higher steam ratios. It must be noted that the optimizer moves towards low purge time and low adsorption time for maximum productivity and minimum steam ratios. The scales of these graphs are constructed as per the decision variable range. There is a trade-off between low purge times required for high productivity while maintaining high recovery.

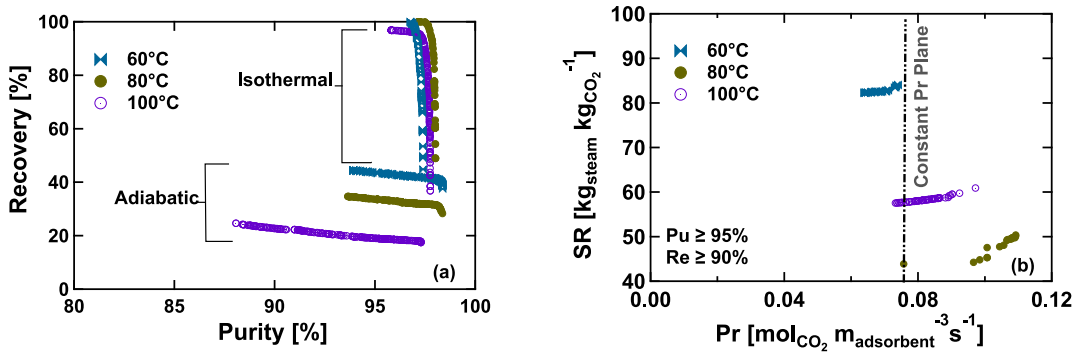

Figure 10: Results of process optimization for varying feed temperatures under isothermal and adiabatic modes of operations. Pareto curves obtained from (a) simultaneous maximization of purity-recovery optimization for varying feed temperatures under adiabatic and isothermal modes of operation, and (b) Pareto curves obtained from steam ratio-productivity optimization for varying feed temperatures under isothermal mode of operation.

A cycle optimization was carried out to understand the effect of feed temperatures and the results are demonstrated in Fig. 10. From Fig. 10(a), it is observed that, under the adiabatic operation, the optimized CO_2 recoveries at a feed temper-

ature of 60 °C are 40 - 50%, 30 - 40% for 80 °C and 15 - 25% for 100 °C. It is clear that, a lower feed temperature improves the process performance in an adiabatic scenario. Although high purities are achievable, high recoveries cannot be achieved for the flue gas temperatures of 60 °C - 110 °C in an adiabatic mode of operation. This means that, although the optimizer searches thousands of operating conditions, none satisfy the purity and recovery constraints for any feed temperatures for the 3-step SA-TSA process. This is attributed to the difference in CO_2 capacity for different feed temperatures. The results from cycle optimization confirm the results discussed in section 4.2 and 4.4. From Fig. 10(a) it can be observed that the optimized paretos under isothermal mode of operation is unaffected by feed temperature. This implies that, in addition to high purities, high recoveries are achievable for the considered temperature range of NGCC flue gas in an isothermal scenario for the 3-step SA-TSA process. The high recoveries are due to the preserved CO_2 capacity, as the column has no moving heat fronts. The corresponding optimized steam ratios and productivity that satisfy a purity constraint of $\geq 95\%$ and a recovery constraint of $\geq 90\%$ for different feed temperatures is seen in Fig. 10(b). From Fig. 10(b) the highest steam ratio of 80 - 90 $\mathrm{kg_{steam}\,kg_{CO_2}^{-1}}$ and lowest productivity of 0.06 - 0.08 $\mathrm{mol_{CO_2}\,m_{adsorbent}^{-3}\,s^{-1}}$ is seen for a feed temperature of 60 °C. This is followed by a stream ratio of 50 - 60 $\mathrm{kg_{steam}\,kg_{CO_2}^{-1}}$ and productivity of 0.07 - 0.1 $\mathrm{mol_{CO_2}\,m_{adsorbent}^{-3}\,s^{-1}}$ for 100 °C. The lowest steam ratio and highest productivity of 40 - 50 $\mathrm{kg_{steam}\,kg_{CO_2}^{-1}}$ and 0.1 - 0.12 $\mathrm{mol_{CO_2}\,m_{adsorbent}^{-3}\,s^{-1}}$ for a feed temperature of 80 °C. It appears that the trend in the steam ratio-productivity for different feed temperatures is not monotonic. In order to understand the observations, a plane of constant productivity, of 0.075 $\mathrm{mol_{CO_2}\,m_{adsorbent}^{-3}\,s^{-1}}$ is considered, and the corresponding operating conditions are compared in Table 4. It can be seen that purity and recovery values across different feed temperatures are comparable. The variation of steam ratios across different feed temperatures is attributed to adsorption times and purge times. Additionally, the steam ratio is a function of steam temperature, recovery, t_{ads}, t_{pur}, v_{ads} and v_{pur}. Since the v_{ads} and v_{pur} values are comparable for a particular feed temperature, this implies that, a low t_{ads} and high t_{pur} will result in high steam-ratios. Hence, the steam ratio for 60 °C is the highest and the lowest

for 80 °C. Although, high recoveries are still achievable in an isothermal mode of operation run with different feed temperatures, the best possible steam consumption is as high as 40 - 50 $kg_{steam}\ kg_{CO_2}^{-1}$. Despite non-active temperature fronts that preserve the capacity of the bed thereby increasing CO_2 recovery, the long purge times that are reflective of the isotherm shape result in increased steam ratios and reduced productivity. That is, despite the material exhibiting ideal adsorbent qualities, the material's performance when subjected to this 3-step SA-TSA process is poor.

Table 4: Process conditions and performance indicators for varying feed temperature under isothermal mode of operation corresponding to Fig. 10(b). All points correspond to a constant productivity of 0.075 $mol_{CO_2}\ m_{adsorbent}^{-3}\ s^{-1}$.

T_{feed} [°C]	t_{ads} [s]	t_{pur} [s]	t_{con} [s]	v_{ads} [$m\ s^{-1}$]	v_{pur} [$m\ s^{-1}$]	v_{con} [$m\ s^{-1}$]	Pu [%]	Re [%]	SR [$kg_{steam}\ kg_{CO_2}{}^{-1}$]
60	823	6868	532	0.92	0.98	0.93	96	91	83
80	1262	6089	1171	0.69	0.63	0.62	97	91	43
100	884	5280	666	0.81	0.74	0.64	96	90	56

4 Conclusion

Mg_2MOF that showed an interesting double-stepped CO_2 isotherm was evaluated as a potential adsorbent for TSA based CO_2 capture from dry NGCC flue gas. A 3-step TSA process with a steam purge was studied. The isotherm was described using an empirical equation. The isotherm parameters and the fixed bed model was used to perform simulations under isothermal, adiabatic and non-isothermal modes of operation, varying feed temperature, and varying heat capacity. Following this, cyclic process simulations were run. Lastly cycle optimization was carried out to identify potential set of operating conditions for maximum purity, recovery, productivity and minimum steam ratio. From these investigations, it can be concluded

that thermal front propagation and high heat of adsorption had a major impact on process dynamics. In the adiabatic mode of operation, the temperature fronts lead to substantial reduction of CO_2 capacity thereby rendering a poor process performance where US-DOE targets of purity and recovery were not met. However, in the isothermal case, where there are no active heat fronts, the capacity of the bed is preserved and hence the process performance satisfies US-DOE targets. Even with the isothermal mode, the cycle optimization resulted in high steam ratio and low productivity. This is attributed to the very long purge times required to regenerate the bed.

It is worth pointing out that Svante Inc. reports a steam ratio 1 - 2 $kg_{steam}\, kg_{CO_2}^{-1}$ for a TSA separating CO_2 from a 16% feed mixture using structured CALF-20 [16]. The productivity reported is around 10.6 $TPD_{CO_2}\, m_{bed}^{-3}$. Our work indicates a low Pr of 0.38 $TPD_{CO_2}\, m_{bed}^{-3}$ despite a high working capacity of $\approx$2 $mol\, kg^{-1}$ reported for the material. The disparity in values is owed to the process cycle times. Svante Inc. reports a cycle time of 52 s owing to the rapid TSA process design unlike our traditional TSA process design with a high cycle time of 6000 s. Despite high recoveries and purities that can be obtained in an isothermal scenario for the 3-step SA-TSA, there is scope for process design improvement by including appropriate contactors.

The study emphasizes the importance of evaluating novel CO_2 capture materials under realistic process conditions, as simplified estimates based on isotherms alone does not reveal the inherent complexities; an approach that is gaining attention, particularly in the CO_2 capture community [35–37]. In fact, the unusual isotherm shape which at the outset seems to have advantages results in the propagation of thermal fronts that leads to reduced bed capacity resulting in unusualy low recoveries. For such systems, the study reveals that heat management will be critical in ensuring that the bed capacity is maintained. As scale-up studies are considered for such systems, the complexities of designing contactors that will allow for such schemes need to be explored [38].

Acknowledgments

We thank James Sawada and Kasturi Nagesh Pai, University of Alberta for their inputs. We acknowledge the funding from TOTALEnergies and MITACS through the Adsorptive CO_2 removal from dilute sources (ACO_2RDS) project. Computational work reported in this study were supported by Digital Research Alliance of Canada through the Resources for Research groups grant.

Declaration of Interests

The authors confirm that there is no conflict of interest to declare. One of the funders, TOTALEnergies, has active CO_2 capture and storage projects.

Supporting Information

Supporting information related to this article can be found online at ***. The study of the effect of heat transfer for various feed composition, effect of density and the spread of decision variable space for process optimization.

Nomenclature

Roman symbols

b	temperature dependent fitting parameter [bar^{-1}]
C	concentration [mol m^{-3}]
C_p	heat capacity [J kg^{-1} K^{-1}]
D_m	molecular diffusivity [m^2 s^{-1}]
D_L	axial dispersion [m^2 s^{-1}]
h	heat transfer coefficient [W m^{-2} K^{-1}]
J	objective function [-]
k	LDF coefficient [s^{-1}]
K_z	effective gas thermal conductivity [W m^{-1} K^{-1}]
L	length of column [m]
m_1	temperature dependent fitting parameter [bar]
m_2	temperature dependent fitting parameter [bar]
ΔH	heat of adsorption [kJ mol^{-1}]
P	pressure [bar]
Pr	productivity [$\mathrm{mol}_{\mathrm{co_2}}$ $\mathrm{m}^{-3}_{\mathrm{adsorbent}}$ s^{-1}]
Pu	purity [%]
q	solid phase loading [mol kg^{-1}]
q^*	equilibrium solid phase loading [mol kg^{-1}]
Q	volumetric flow [m^3 s^{-1}]
r	radius [m]
R	universal gas constant [Pa m^3 mol^{-1} K^{-1}]
Re	recovery [%]
s_1	temperature dependent fitting parameter [bar^{-1}]
SR	steam ratio [$\mathrm{kg}_{\mathrm{steam}}$ $\mathrm{kg}^{-1}_{\mathrm{CO_2}}$]
t	time [s]

T	temperature [K]
v	velocity [m s^{-1}]
V	volume [m^3]
y	mole fraction [-]
z	axial coordinate [m]

Greek symbols

ϵ	voidage [-]
μ	fluid viscosity [kg m^{-1} s^{-1}]
ρ	density [kg m^{-3}]

Abbreviations, subscripts and superscripts

ads	adsorption
feed	feed
pur	purge
con	conditioning
in	inside
out	outside
i	index of species
w	wall
p	particle
s	solid
a	ambient
t	time

Acronyms

GA	genetic algorithm
NGCC	natural gas combined cycle
NSGA	non-dominated sorting genetic algorithm
PSA	pressure swing adsorption
TSA	temperature swing adsorption
SA-TSA	steam assisted temperature swing adsorption
CCS	carbon capture and storage
CSS	cyclic steady state
MOF	metal organic framework
Mg_2MOF	Mg_2(dobpdc)(tetramine)
ODE	ordinary differential equation
PDE	partial differential equation
SSL	single-site Langmuir model

References

[1] IPCC, "Synthesis Report. Contribution of Working Groups I, II and III to the Fifth Assessment Report of the Intergovernmental Panel on Climate Change," tech. rep., 2014.

[2] M. Bui, C. S. Adjiman, A. Bardow, E. J. Anthony, A. Boston, S. Brown, P. S. Fennell, S. Fuss, A. Galindo, L. A. Hackett, J. P. Hallett, H. J. Herzog, G. Jackson, J. Kemper, S. Krevor, G. C. Maitland, M. Matuszewski, I. S. Metcalfe, C. Petit, G. Puxty, J. Reimer, D. M. Reiner, E. S. Rubin, S. A. Scott, N. Shah, B. Smit, J. P. M. Trusler, P. Webley, J. Wilcox, and N. Mac Dowell, "Carbon capture and storage (CCS): the way forward," *Energ. Environ. Sci.*, vol. 11, no. 5, pp. 1062–1176, 2018.

[3] NETL, "Current and Future Technologies for Natural Gas Combined Cycle (NGCC) Power Plants," tech. rep., 2013.

[4] D. Y. Leung, G. Caramanna, and M. M. Maroto-Valer, "An Overview of Current Status of Carbon Dioxide Capture and Storage Technologies," *Renew. Sust. Energ. Rev.*, vol. 39, pp. 426–443, 2014.

[5] D. M. Ruthven, *Principles of adsorption and adsorption processes*. New York: John Wiley, 1984.

[6] R. T. Yang, *Gas Separation by Adsorption Processes*. Imperial College Press, 1997.

[7] K. N. Pai, V. Prasad, and A. Rajendran, "Practically Achievable Process Performance Limits for Pressure-Vacuum Swing Adsorption-based Postcombustion CO_2 Capture," *ACS Sustain. Chem. Eng.*, vol. 9, no. 10, pp. 3838–3849, 2021.

[8] S. G. Subraveti, S. Roussanaly, R. Anantharaman, L. Riboldi, and A. Rajendran, "How much can novel solid sorbents reduce the cost of post-combustion CO_2 capture? a techno-economic investigation on the cost limits of pressure–vacuum swing adsorption," *Appl. Energ.*, vol. 306, p. 117955, 2022.

[9] G. Hofer, J. Fuchs, G. Schöny, and T. Pröll, "Heat Transfer Challenge and Design Evaluation for a Multi-Stage Temperature Swing Adsorption Process," *Powder Technol.*, vol. 316, pp. 512–518, 2017.

[10] K. S. Knaebel, "CO_2 Capture by Moving Bed Temperature Swing Adsorption," in *AIChE Annual Meeting, Conference*, 2008.

[11] C. Dhoke, A. Zaabout, S. Cloete, and S. Amini, "Review on Reactor Configurations for Adsorption-based CO_2 Capture," *Ind. Eng. Chem. Res.*, vol. 60, no. 10, pp. 3779–3798, 2021.

[12] S. Van Paasen, M. Infantino, J. Yao, S. H. Leenders, J. M. van de Graaf, A. Klingler, F. Zerobin, T. Pröll, G. Schöny, J. Fuchs, *et al.*, "Development of the solid sorbent technology for post combustion CO_2 capture towards commercial prototype," *Int. J. of Greenh. Gas Con.*, vol. 109, p. 103368, 2021.

[13] A. Samanta, A. Zhao, G. K. Shimizu, P. Sarkar, and R. Gupta, "Post-Combustion CO_2 Capture using Solid Sorbents: A Review," *Ind. Eng. Chem. Res*, vol. 51, no. 4, pp. 1438–1463, 2012.

[14] R. L. Siegelman, E. J. Kim, and J. R. Long, "Porous materials for carbon dioxide separations," *Nature Mat.*, vol. 20, no. 8, pp. 1060–1072, 2021.

[15] J.-B. Lin, T. T. T. Nguyen, R. Vaidhyanathan, J. Burner, J. M. Taylor, H. Durekova, F. Akhtar, R. K. Mah, O. Ghaffari-Nik, S. Marx, N. Fylstra, S. S. Iremonger, K. W. Dawson, P. Sarkar, P. Hovington, A. Rajendran, T. K. Woo, and G. K. H. Shimizu, "A scalable metal-organic framework as a durable physisorbent for carbon dioxide capture," *Science*, vol. 374, no. 6574, pp. 1464–1469, 2021.

[16] P. Hovington, O. Ghaffari-Nik, L. Mariac, A. Liu, B. Henkel, and S. Marx, "Rapid cycle temperature swing adsorption process using solid structured sorbent for CO_2 capture from cement flue gas," in *Proceedings of GHGT-15*, 2021.

[17] T. M. McDonald, J. A. Mason, X. Kong, E. D. Bloch, D. Gygi, A. Dani, V. Crocellà, F. Giordanino, S. O. Odoh, W. S. Drisdell, B. Vlaisavljevich, A. L. Dzubak, R. Poloni, S. K. Schnell, N. Planas, K. Lee, T. Pascal, L. F. Wan, D. Prendergast, J. B. Neaton, B. Smit, J. B. Kortright, L. Gagliardi, S. Bordiga, J. A. Reimer, and J. R. Long, "Cooperative Insertion of CO_2 in Diamine-Appended Metal-Organic Frameworks," *Nature*, vol. 519, no. 7543, pp. 303–308, 2015.

[18] E. J. Kim, R. L. Siegelman, H. Z. H. Jiang, A. C. Forse, J.-H. Lee, J. D. Martell, P. J. Milner, J. M. Falkowski, J. B. Neaton, J. A. Reimer, S. C. Weston, and J. R. Long, "Cooperative Carbon Capture and Steam Regeneration with Tetraamine-Appended Metal–Organic Frameworks," *Science*, vol. 369, no. 6502, pp. 392–396, 2020.

[19] M. Hefti, L. Joss, Z. Bjelobrk, and M. Mazzotti, "On the Potential of Phase-Change Adsorbents for CO_2 Capture by Temperature Swing Adsorption," *Faraday Discuss.*, vol. 192, pp. 153–179, 2016.

[20] K. N. Pai, J. D. Baboolal, D. A. Sharp, and A. Rajendran, "Evaluation of Diamine-Appended Metal-Organic Frameworks for Post-Combustion CO_2 Capture by Vacuum Swing Adsorption," *Sep. Purif. Technol.*, vol. 211, pp. 540–550, 2019.

[21] J. Fujiki, H. Kajiro, Y. Takakura, T. Yajima, and Y. Kawajiri, "Breakthrough analysis for parameter estimation of CO 2 adsorption on pelletized flexible metal – organic framework," *J. Chem. Eng.*, vol. 460, no. November 2022, p. 141781, 2023.

[22] Y. Takakura, S. Sugimoto, J. Fujiki, H. Kajiro, T. Yajima, and Y. Kawajiri, "Model-based analysis of a highly efficient co2 separation process using flexible metal–organic frameworks with isotherm hysteresis," *ACS Sustainable Chemistry & Engineering*, vol. 10, no. 45, pp. 14935–14947, 2022.

[23] R. Hughes, G. Kotamreddy, A. Ostace, D. Bhattacharyya, R. L. Siegelman, S. T. Parker, S. A. Didas, J. R. Long, B. Omell, and M. Matuszewski, "Isotherm, Ki-

netic, Process Modeling, and Techno-Economic Analysis of a Diamine-Appended Metal–Organic Framework for CO_2 Capture using Fixed Bed Contactors," *Energy Fuels*, vol. 35, no. 7, pp. 6040–6055, 2021.

[24] M. Clausse, J. Merel, and F. Meunier, "Numerical Parametric Study on CO_2 Capture by Indirect Thermal Swing Adsorption," *Int. J. Greenh. Gas Con.*, vol. 5, no. 5, pp. 1206–1213, 2011.

[25] A. Ntiamoah, J. Ling, P. Xiao, P. A. Webley, and Y. Zhai, "CO_2 Capture by Temperature Swing Adsorption: Use of Hot CO_2-Rich Gas for Regeneration," *Ind. Eng. Chem. Res.*, vol. 55, no. 3, pp. 703–713, 2016.

[26] V. Stampi-Bombelli, M. Van Der Spek, and M. Mazzotti, "Analysis of Direct Capture of CO_2 from Ambient Air via Steam-Assisted Temperature–Vacuum Swing Adsorption," *Adsorption*, vol. 26, pp. 1183–1197, 2020.

[27] L. W. Bingel and K. S. Walton, "Surprising use of the business innovation bass diffusion model to accurately describe adsorption isotherm types i, iii, and v," *Langmuir*, vol. 39, no. 12, pp. 4475–4482, 2023.

[28] R. Haghpanah, A. Majumder, R. Nilam, A. Rajendran, S. Farooq, I. A. Karimi, and M. Amanullah, "Multiobjective Optimization of a Four-Step Adsorption Process for Postcombustion CO_2 Capture via Finite Volume Simulation," *Ind. Eng. Chem. Res.*, vol. 52, no. 11, pp. 4249–4265, 2013.

[29] D. M. Ruthven and C. B. Ching, "Counter-Current and Simulated Counter-Current Adsorption Separation Processes," *Chem. Eng. Sci.*, vol. 44, no. 5, pp. 1011–1038, 1989.

[30] K. Deb, A. Pratap, S. Agarwal, and T. Meyarivan, "A Fast and Elitist Multiobjective Genetic Algorithm: NSGA-II," *IEEE Trans. Evol. Comput.*, vol. 6, no. 2, pp. 182–197, 2002.

827 [31] M. Mazzotti and A. Rajendran, "Equilibrium Theory–based Analysis of Non-
828 linear Waves in Separation Processes," *Annu. Rev. Chem. Biomol. Eng.*, vol. 4,
829 no. 1, pp. 119–141, 2013.

830 [32] H. K. Rhee, R. Aris, and N. R. Amundson, *First-order partial differential equa-*
831 *tions*, vol. I. Mineola, N.Y.: Dover Publications, 2001.

832 [33] R. L. Siegelman, P. J. Milner, A. C. Forse, J. H. Lee, K. A. Colwell, J. B. Neaton,
833 J. A. Reimer, S. C. Weston, and J. R. Long, "Water Enables Efficient CO_2
834 Capture from Natural Gas Flue Emissions in an Oxidation-Resistant Diamine-
835 Appended Metal-Organic Framework," *J. Am. Chem. Soc*, vol. 141, no. 33,
836 pp. 13171–13186, 2019.

837 [34] S. M. Moosavi, B. Á. Novotny, D. Ongari, E. Moubarak, M. Asgari, Ö. Kadioglu,
838 C. Charalambous, A. Ortega-Guerrero, A. H. Farmahini, L. Sarkisov, S. Garcia,
839 F. Noé, and B. Smit, "A data-science approach to predict the heat capacity of
840 nanoporous materials," *Nat. Mater*, vol. 21, no. 12, pp. 1419–1425, 2022.

841 [35] A. K. Rajagopalan, A. M. Avila, and A. Rajendran, "Do adsorbent screening
842 metrics predict process performance? a process optimisation based study for
843 post-combustion capture of co2," *Int. J. Greenh. Gas Con.*, vol. 46, pp. 76–85,
844 2016.

845 [36] M. Taddei and C. Petit, "Engineering metal–organic frameworks for adsorption-
846 based gas separations: From process to atomic scale," *Molecular Systems Design*
847 *& Engineering*, vol. 6, no. 11, pp. 841–875, 2021.

848 [37] A. H. Farmahini, S. Krishnamurthy, D. Friedrich, S. Brandani, and L. Sarkisov,
849 "Performance-based screening of porous materials for carbon capture," *Chem.*
850 *Rev.*, vol. 121, no. 17, pp. 10666–10741, 2021.

851 [38] Y. Fan, R. P. Lively, Y. Labreche, F. Rezaei, W. J. Koros, and C. W.
852 Jones, "Evaluation of CO_2 adsorption dynamics of polymer/silica supported

poly(ethylenimine) hollow fiber sorbents in rapid temperature swing adsorption," *Int. J. Greenh. Gas Con.*, vol. 21, pp. 61–71, 2014.